Article

Effect Mechanism of *α*-Ferrite Sustained Precipitation on High-Temperature Properties in Continuous Casting for Peritectic Steel

Songyuan Ai [1], Yifan Li [1], Mujun Long [1,2,*], Haohao Zhang [1], Dengfu Chen [1], Huamei Duan [1], Danbin Jia [1,*] and Bingzhi Ren [3]

1   Laboratory of Materials and Metallurgy, College of Materials Science and Engineering, Chongqing University, Chongqing 400044, China; asy@cqu.edu.cn (S.A.); 20192859@cqu.edu.cn (Y.L.); 201909021107@cqu.edu.cn (H.Z.); chendfu@cqu.edu.cn (D.C.); duanhuamei@cqu.edu.cn (H.D.)
2   National Key Laboratory of Advanced Casting Technologies, Chongqing University, Chongqing 400044, China
3   School of Metallurgy and Materials Engineering, Chongqing University of Science and Technology, Chongqing 401331, China; renbingzhi@cqust.edu.cn
*   Correspondence: longmujun@cqu.edu.cn (M.L.); jiadanbin@cqu.edu.cn (D.J.)

Abstract: Exploring the mechanism of the *α*-ferrite precipitation process on high-temperature properties plays an important guiding role in avoiding slab cracks and effectively regulating quality. In this work, in situ observation of the *α*-ferrite sustained precipitation behavior for peritectic steel during the austenitic phase transition process has been investigated using high-temperature confocal scanning laser microscopy. Meanwhile, the high-temperature evolution of the phase fractions during the phase transition process was quantitatively analyzed based on the high-temperature expansion experiment using the peak separation method. Furthermore, the high-temperature properties variations of the casting slab during the *α*-ferrite sustained precipitation process were investigated with the Gleeble thermomechanical simulator. The results show that the film-like ferrite precipitated along the austenite grain boundaries at the initial stage of phase transition, then needle-like ferrite initiates rapid precipitation on film-like ferrite when the average thickness reaches 15~20 μm. Hot ductility reached a minimum at the ferrite phase fraction f_α = 10~15%, while high-temperature properties returned to a higher level after f_α > 40~45%. The appearance of a considerable amount of needle-like ferrite and grain refinement effectively improves the high-temperature properties with the *α*-ferrite precipitation process advances.

Keywords: *α*-ferrite sustained precipitation; phase fraction; hot ductility; high-temperature strength; effect mechanism

1. Introduction

Peritectic steel is widely used in mechanical equipment, automotive parts, building structural materials, ship hulls, and other manufacturing processes due to the advantages of excellent toughness, processability, weldability, and lower material and process costs [1–3]. However, cracks in the continuous casting process have always been an important factor in troubling and limiting the development of peritectic steel [4,5]. Frequent cracks in the corners and surfaces of slabs significantly deteriorate the quality of steel products and directly lead to product obsolescence, which brings serious economic losses. Therefore, eliminating cracks and further enhancing the toughness in continuous casting of peritectic steel has become an important priority, along with the growing demand for high-quality steel products.

The formation of cracks is closely related to the evolution of the microstructure stage and mechanical properties of the slab during the high-temperature continuous casting process [6–8]. Brimacombe et al. [9] and Suzuki et al. [10,11] indicated the presence of

three typical brittle zones in the hot ductility evolution during the continuous casting process. On this basis, many researchers have explored the causes and mechanisms of hot ductility degradation of continuous casting slabs within the third brittle zone. Considerable research [12–16] has shown that in the temperature range of continuous casting production, microalloying elements, such as Nb, Ti, and V, easily form carbides, nitrides, or carbonitrides and precipitate at austenite grain boundaries. Under applied external force or deformation conditions, the stress level or strain concentration increased in the vicinity of the precipitates, which led to a rapid deterioration of the as-cast slab hot ductility [17]. Additionally, Thomas et al. [18] and Mintz et al. [19] pointed out that film-like proeutectoid ferrite forms at austenite grain boundaries were another important reason for the deterioration of properties. Evidently, since the strength of ferrite was only about 25% of that of austenite, the stress or strain concentration occurs on the ferrite film at the austenite grain boundaries during deformation, which caused the crack initiation and extension [20–22]. Yang et al. [23] investigated that the cast slab hot ductility decreases with increasing thickness of film-like ferrite after exceeding 5 μm. Mintz et al. [24–27] proposed that the deformation-induced ferrite appearing at austenite grain boundaries near the A_{e3} temperature leads to a decrease in hot ductility, with the effect being particularly significant when the thickness of the ferrite film reached 20 μm. Qian et al. [28] concluded that the ferrite film thickness presented poor uniformity at the beginning of the austenite-ferrite phase transformation as the growth rate of ferrite accelerates, which contributed to the rapid decrease in the reduction of area (R_A) value. Liu et al. [29] characterized the crack generation and extension during the austenite phase transition of niobium microalloyed steel and discussed the synergistic mechanism of ferrite precipitation relative to cracks. Overall, these studies primarily focus on the effect of the formation and distribution of film-like ferrite on hot ductility in the pre-austenite phase transition stage, with fewer quantitative descriptions of the properties evolution during the whole α-ferrite precipitation advancement process. Actually, as the austenite phase transition process advances, the microstructure of the as-cast slab undergoes complex changes such as the generation of new phases, the depletion of the original phases, and the change in the crystal structure of the matrix phases [30,31], which has a substantial impact on the properties [32,33]. Furthermore, avoiding cracks is only a basic requirement for high-quality steel products, and further improvements in strength and toughness should be considered as a new aim. In other words, elucidating the evolution of strength indexes during the α-ferrite precipitation process is equally important. Unfortunately, researchers seem to emphasize excessively on the hot ductility while neglecting attention to the evolution of high-temperature strength.

In this work, a high-temperature confocal scanning laser microscopy (HTCSLM) has been employed to observe the whole process of austenite phase transition during continuous casting. Moreover, a high-temperature expansion meter has quantified the phase fraction of each matrix phase as a function of temperature during the austenite phase transition. Meanwhile, the high-temperature properties at different temperatures have been simulated and obtained with the aid of a Gleeble thermomechanical simulator during the α-ferrite precipitation process. This investigation aims to clarify the effect mechanism of the α-ferrite sustained precipitation on the high-temperature properties, which provides theoretical instructions for the avoidance of as-cast slab cracks and high-quality steel production.

2. Materials and Methods

The experimental material used in this study was a peritectic casting slab with 230 mm in thickness, which was collected from a commercial steel plant. The chemical compositions of the casting slab in mass fraction (wt%) were listed as follows: 0.15 C, 0.21 Si, 1.08 Mn, 0.017 P, 0.002 S, 0.03 Ni, 0.05 Cr, 0.053 Ti, 0.008 Nb, and 0.004 N. As shown in Figure 1a, all specimens have been machined from the casting slab with the axes parallel to the casting direction, and the sample locations were around 10 mm below the surface and more than 100 mm away from the narrow face. The dimensions of

the specimens for the high-temperature experiments are shown in Figure 1b. The specimens for high-temperature in situ observation have been processed into thin cylinders of φ 7.8 mm × 2 mm. The dimension of cylindrical high-temperature expansion specimens was φ 4.0 mm × 25 mm. Subsequently, the specimens for high-temperature tensile tests were machined into φ 10 mm × 120 mm round bars with M10 threads at both ends.
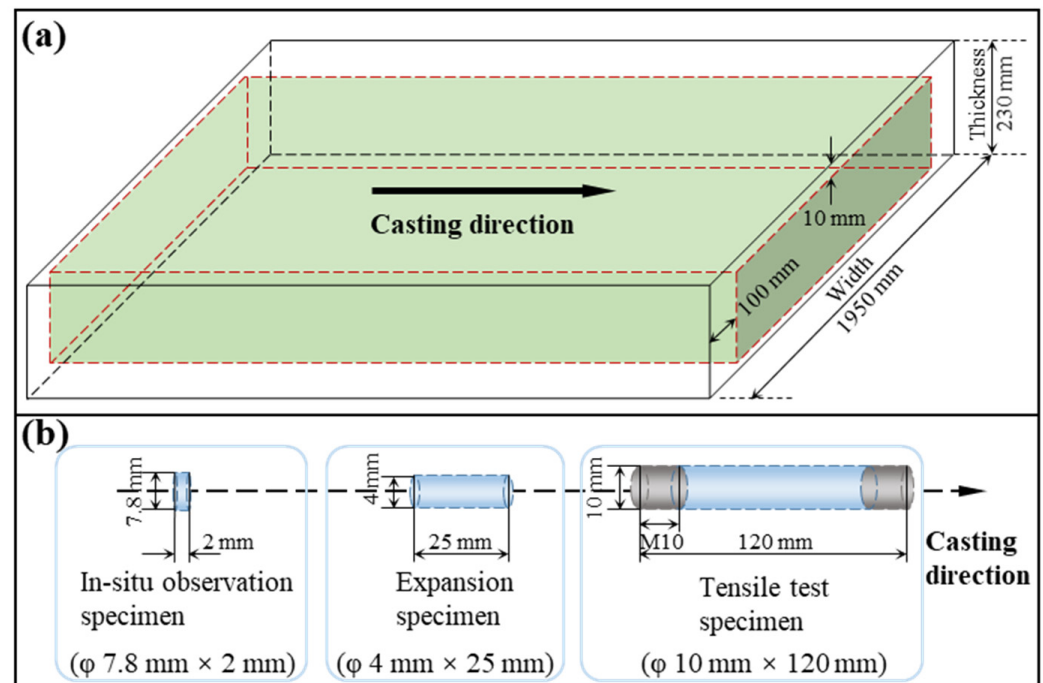

Figure 1. Schematic diagram of the position and dimension for experimental specimens: (**a**) Position of specimen processing; (**b**) specimen dimensions for the high-temperature experiment.

Before the experiments, the upper and lower surfaces of the cylindrical specimens of in situ observation and high-temperature expansion were ground using a grinding and polishing machine. Then, 0.5 μm diamond spray polishing compounds were employed for mechanical polishing. All specimens for high-temperature experiments were ultrasonically cleaned in anhydrous ethanol to remove impurities adhering to the surface. Finally, these specimens have been dried and examined.

The whole process of austenite phase transition in the cooling process was simulated experimentally using a HTCLSM (Yonekura, Osaka, Japan), which includes a confocal scanning laser microscope and an infrared image furnace. A standard observation experiment includes a heating and cooling cycle under a high-purity argon gas. The specimen was heated and cooled using IR radiation and gas circulation. The temperature was continuously recorded using the R-type thermocouple installed below the Pt-specimen holder—the detailed experimental steps for HTCSLM observation are shown in Figure 2a. To simulate the continuous casting process, the sample was heated to 1350 °C from room temperature with 600 °C/min to dissolve precipitates such as carbon nitrides and AlN as much as possible. Next, the heating specimen was held for 10 min at 1350 °C to obtain a coarse grain size similar to the as-cast structure. The phase transition behavior mainly depended on the cooling conditions of the slab in the secondary cooling zone of continuous casting, which was related to the process parameters such as casting speed, steel type and size, as well as cooling intensity. Combined with the practical production of continuous casting and the current studies, a cooling rate consistent with conventional continuous casting slab (i.e., 100 °C/min [34–36]) was employed to observe the whole process of α-ferrite precipitation.
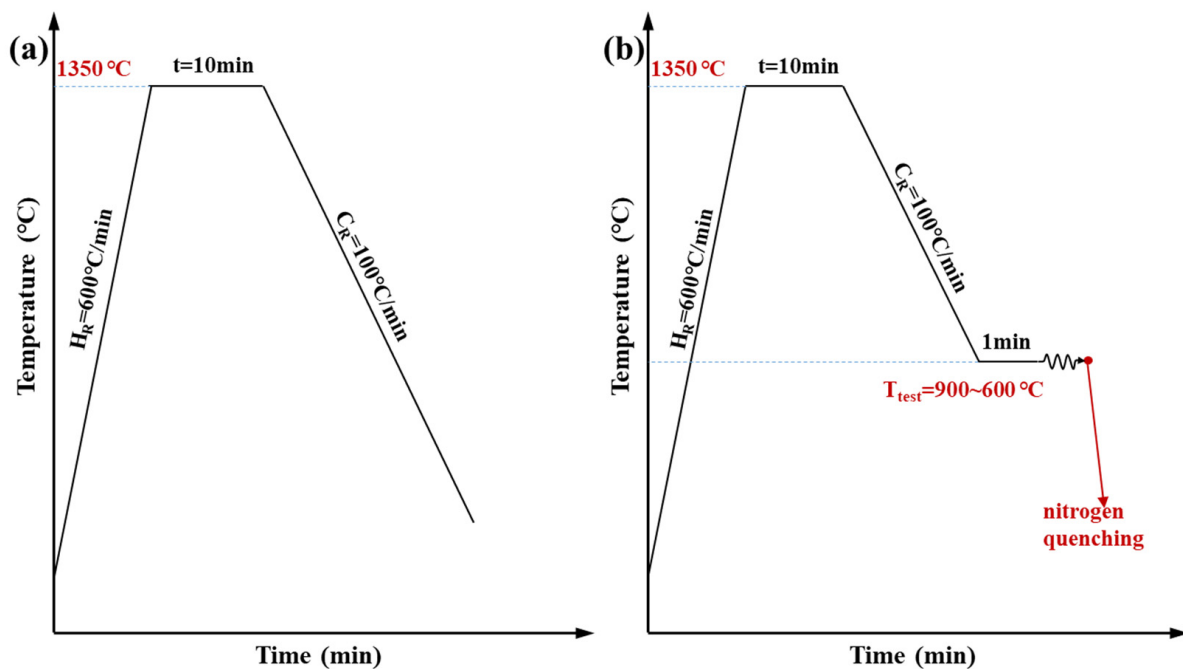
Figure 2. Diagram of the experimental scheme: (**a**) In situ observation and high-temperature expansion analysis; (**b**) high-temperature thermal tensile analysis.

Moreover, the high-temperature expansion experiment was the most effective method to quantitatively analyze the austenite phase transition behavior due to its simplicity and high accuracy. The quantitative description of the phase fraction changes during the austenite phase transition was accomplished with the aid of the DIL high-temperature dilatometer (Netzsch, Waldkraiburg, Germany), and the thermal history of the specimen changes in perfect agreement with the in-situ observed experiment. During the measurement process, these cylindrical specimens were clamped between two quartz push rods. A linear variable displacement transducer was used to record the length changes between the small cylindrical specimen and the push rods due to thermal expansion or contraction occurrence in the specimen interior. The cylindrical specimen was heated through an induction coil. In particular, the experimental process was protected by argon gas throughout to avoid oxidation of the samples. Finally, the specimen at the end of the expansion experiment was further characterized using optical microscopy with 4% nitric solution etching.

In addition, mechanical properties were tested at different temperatures using Gleeble (DIS, Burbank, CA, USA), and the investigation protocol is shown in Figure 2b. The detailed experimental steps for high-temperature thermal tensile experiments were as follows. The specimens were heated to 1350 °C from room temperature with a rapid heating rate of 600 °C/min. And then, the heating specimen was held for 10 min to homogenize. Next, the specimen was continuously cooled to test the temperature (T_{test}) ranging between 600 °C and 900 °C with a cooling rate of 100 °C/min. Before the deformation, the specimen was kept for 1 min at test temperatures to have even temperature fields. Next, tensile tests were carried out at a constant strain rate of 5×10^{-3} s^{-1} until complete failure. Particularly, this smaller strain rate was similar to the one experienced by the slab surface during the unbending operation in continuous casting [37,38]. Finally, the specimens were quickly cooled to room temperature using nitrogen gas after fracture in order to preserve their structure at high temperatures. It should be noted that the tensile experiment was repeated three times for each test temperature to eliminate the effects of errors in the testing process on the results. Meanwhile, the fracture morphology was observed using scanning electron microscopy (JEOL, Tokyo, Japan), and the microstructure was investigated using optical microscopy after 4% nitric acid-alcohol etching.

3. Results and Discussion

3.1. In Situ Observation of Microstructure Evolution during the Whole α-Ferrite Precipitation Process

Mastering the evolution of the microstructure process of austenite decomposition is the foundation for quantitatively describing the behavior of phase transition. Figure 3 illustrates the microstructure variation during the sustained precipitation of α-ferrite in the slab. Large-size austenite grains are prominently visible above 800 °C. As the temperature decreases to around 796 °C, film-like ferrite is the first to be revealed at the austenite grain boundaries, as shown by the arrows in Figure 3b. As the α-ferrite precipitation process advances, needle-like ferrite grows rapidly on the film-like ferrite when the average thickness reaches 15~20 μm, as highlighted by the red dashed circle in Figure 3c. In the temperature range of 650~750 °C, the content of needle-like ferrites increases rapidly, and "bridging" occurs between neighboring needle-like ferrites, as depicted in Figure 3c–e. While the temperature is reduced to below 650 °C, austenite to ferrite transformation is essentially complete, and significant changes in the microstructure of the slab specimen become difficult to observe.
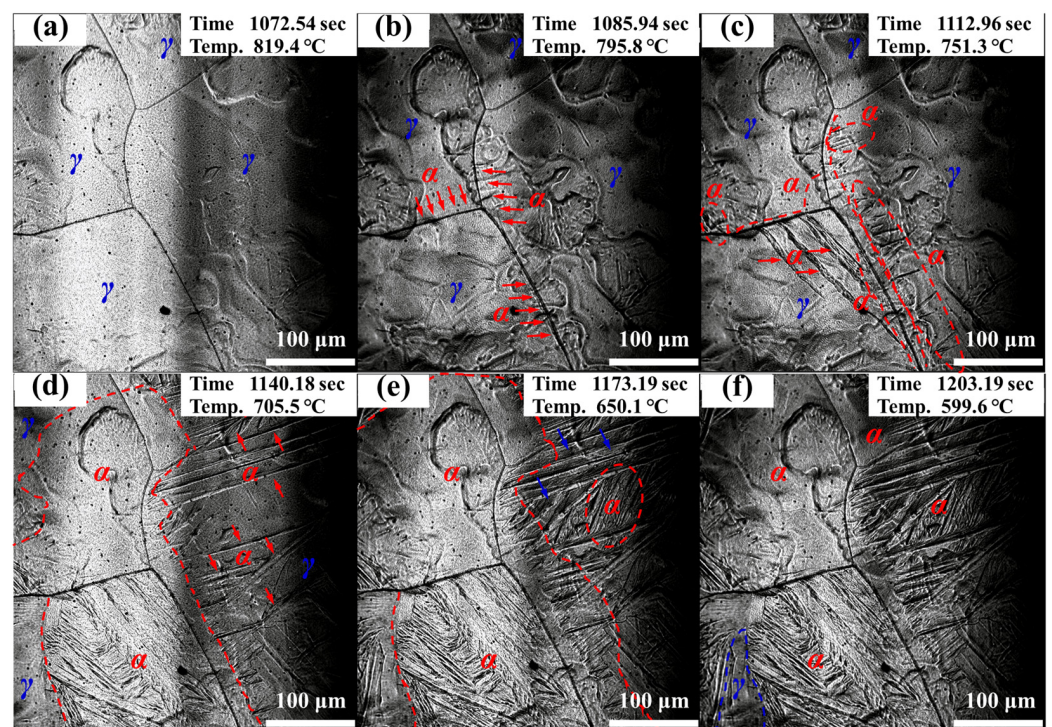

Figure 3. Microstructure evolution during the whole process of α-ferrite precipitation for the slab: (**a**) 819.4 °C; (**b**) 795.8 °C; (**c**) 751.3 °C; (**d**) 699.3 °C; (**e**) 650.1 °C; (**f**) 599.6 °C.

3.2. Critical Temperatures and Phase Fractions for α-Ferrite Precipitation Processes

Generally, the austenite phase transition is accompanied by a significant volume expansion associated with changes in the lattice structure [8,30,39]. This significant dimensional change on the dilation curve can be observable. Based on the isotropic assumption of volume expansion, the length change depends on the internal atomic volume variation. Thus, this relationship can be described by Equation (1):

$$\frac{\Delta V}{V_0} = \frac{V_T - V_0}{V_0} = \frac{\Delta L}{L_0} = \frac{L_T - L_0}{L_0} \tag{1}$$

where V_0 and ΔV are the initial atomic volume and volume increment, and V_T is the atomic volume at temperature T. L_0 and ΔL are the initial specimen length and length increment, and L_T is the specimen length at temperature T.

In our previous study, to achieve more accurate phase fractions at specific temperatures during the austenite phase transition process, we converted the dilation curves into linear thermal expansion coefficient (LTEC) curves. Subsequently, we employed the peak separation method to quantitatively characterize the changes in each phase fraction [30,40]. The linear thermal expansion coefficient (β) can be quantitatively calculated from Equation (2) based on the measured expansion curves:

$$\beta(T) = \frac{1}{L_T} \cdot \frac{dL_T}{dT} \tag{2}$$

where dL_T and dT are the length change of the sample and the corresponding temperature interval, respectively

The dilation curve, linear thermal expansion curve, and the separation results obtained from the high-temperature expansion measurement are shown in Figure 4. As the austenite phase transition process progresses, the crystal structure of the matrix phase gradually transforms from face-centered cubic austenite to body-centered cubic ferrite. The microstructure undergoes four stages: single austenite phase γ, austenite $\gamma \rightarrow$ ferrite α, austenite $\gamma \rightarrow$ pearlite p and $\alpha + p$ biphasic coexistence in sequence. The LTEC curve presents two characteristic transition peaks, representing the ferrite transformation (austenite $\gamma \rightarrow$ pearlite α) and pearlite transformation (austenite $\gamma \rightarrow$ pearlite p), respectively. Figure 4b displays the separation results of the LTEC curve, where A_{r3} and $A_{\alpha f}$ denote the start and finish temperatures of the α-ferrite precipitation, and A_{r1} and A_{pf} represent the start and finish temperatures of the pearlite transition. The four critical temperatures A_{r3}, $A_{\alpha f}$, A_{r1} and A_{pf} are 804 °C, 611 °C, 651 °C and 560 °C, respectively. This generally agrees with the observation in Figure 4, indicating that the temperature interval for austenite phase transition ranges from 560 to 804 °C.
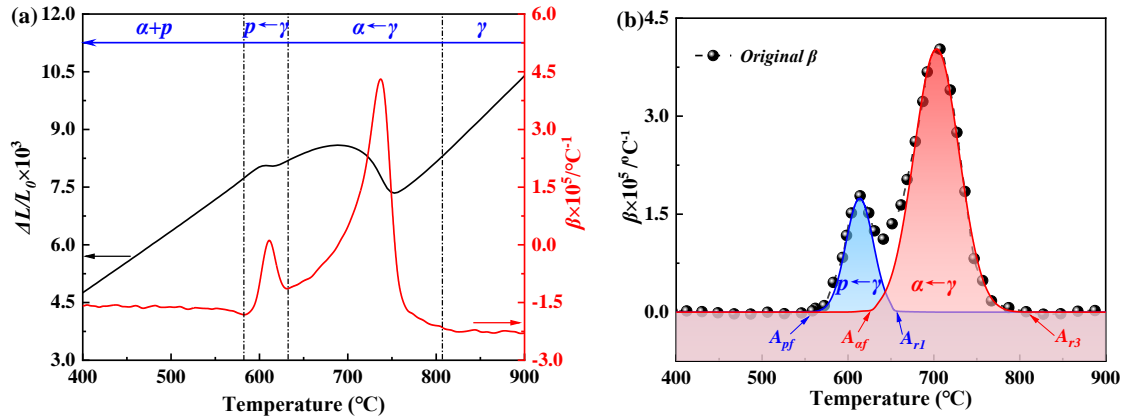

Figure 4. High-temperature expansion behavior of the casting slab during austenite phase transition: (**a**) Dilation curve and LTEC curve; (**b**) Separation results of LTEC curve.

Based on the separation results of the overlapping peaks, the phase fractions of ferrite $f_\alpha(T)$, pearlite $f_p(T)$, and austenite $f_\gamma(T)$ at temperature T can be calculated from Equations (3)–(5) as follows, respectively.

$$f_\alpha(T) = \frac{S_\alpha(T)}{S_{tot}} = \frac{\int_{A_{r3}}^{T(t)} \beta dT}{\int_{A_{r3}}^{A_{pf}} \beta dT}, \quad A_{\alpha f} \leq T(t) \leq A_{r3} \tag{3}$$

$$f_p(T) = \frac{S_p(T)}{S_{tot}} = \frac{\int_{A_{r1}}^{T(t)} \beta dT}{\int_{A_{r3}}^{A_{pf}} \beta dT}, \quad A_{pf} \leq T(t) \leq A_{r1} \tag{4}$$

$$f_\gamma(T) = 1 - f_\alpha(T) - f_p(T), \quad A_{pf} \leq T(t) \leq A_{r3} \tag{5}$$

where $S_\alpha(T)$ and $S_p(T)$ denote the peak area between the baseline and the ferrite and pearlite peak at temperature T, respectively, and S_{tot} denotes the peak area between the baseline and the overlapping peak under the entire LTEC curve.

Figure 5 illustrates the variation of the phase fraction of each phase with temperature during the austenite phase transition. Clearly, the ferrite phase fraction grows slowly at the initial stage of α-ferrite precipitation, at which the ferrite phase fraction is only 12.95% at 750 °C. Accompanying the advancement of the phase transformation process, the ferrite generation rate gradually accelerates, with f_α reaching 58.25% at 700 °C. With a further decrease in temperature, the ferrite transition is essentially complete at 611 °C, where f_α = 77.21%. In addition, the pearlitic transition is completed near 560 °C with a final pearlitic phase fraction f_p = 22.79%. The phase fractions of each phase under typical temperatures are shown in Table 1.
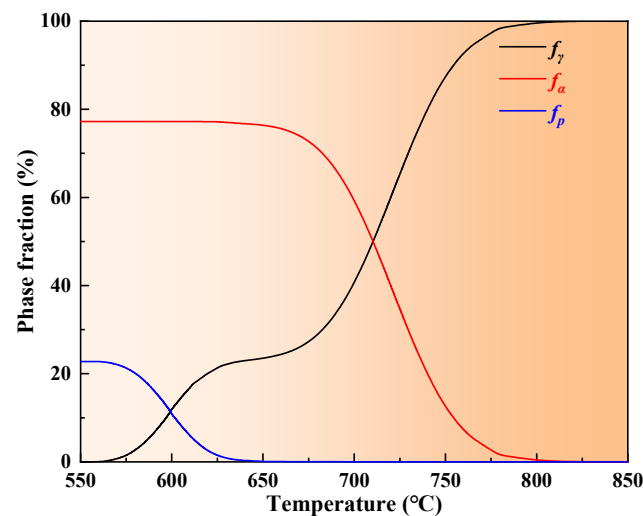

Figure 5. Variations of phase fractions with temperature during austenite phase transition.

Table 1. Phase fractions of each phase at typical temperatures with the austenite phase transition process advances.

Temperature (°C)	Austenite Phase Fraction f_γ (%)	Ferrite Phase Fraction f_α (%)	Pearlite Phase Fraction f_p (%)
900	100	0	0
850	100	0	0
800	99.55	0.45	0
750	87.05	12.95	0
700	40.75	58.25	0
650	23.67	76.27	0.06
600	11.93	77.21	10.86
560	0	77.21	22.79

The microstructure essentially undergoes no further changes after the end of the austenite phase transition, implying that the high-temperature expansion specimen at room temperature can accurately reflect the microstructure state at 560 °C. Figure 6 represents the microstructure of the high-temperature expansion specimen, where the white portion is ferrite and black represents pearlite. The phase fractions of the phases are statistically analyzed using image analysis software (Image-Pro Plus Version 6.0, IPP), and the extensive checks reveal that the ferrite phase fraction is 77.73 ± 0.35%. This indicates that the calculated phase fractions obtained for different temperatures are consistent with the actual austenite phase transition process.

Figure 6. Microstructure of the specimen at the completion of the high-temperature expansion test.

3.3. Evolution of Hot Ductility and High-Temperature Strength during α-Ferrite Precipitation

The stress-strain curve directly reflects the deformation and resistance to the external forces of the material, providing an important reference value for the fracture and mechanical behavior analysis. Figure 7 denotes the engineering and true stress-strain curves of thermal tensile at various temperatures. All specimens exhibit three typical stages: elastic deformation, uniform plastic deformation, and eventual destabilized fracture.

Figure 7. Stress-strain curves at different temperatures during the α-ferrite precipitation process: (**a**) Engineering stress-strain curves; (**b**) true stress-strain curves.

In this work, based on the engineering stress-strain curves, peak strain $\varepsilon_{u,e}$, total elongation $\varepsilon_{f,e}$, reduction of area R_A, and modified energy criterion E_m are adopted to comprehensively measure the hot ductility evolution of the casting slab. It must be noted that the E_m criterion was proposed by Barbier et al. [41] as an alternative to R_A and offers the advantage of circumventing the uncertainty associated with cross-sectional area measurements by directly relying on the energy information in the stress-strain curve. Figure 8 provides the hot ductility variations of the casting slab at different temperatures and ferrite phase fractions, revealing similar trends among the four parameter indices with temperature. The peak strain $\varepsilon_{u,t}$ and total elongation $\varepsilon_{f,t}$ under the true stress-strain curve are also provided as supplementary information in the figure. A typical ductility trough is observed between 700 °C and 850 °C, with the minimum occurring around 750 °C, where $\varepsilon_{u,e}$, $\varepsilon_{f,e}$, R_A, and E_m are 11.44%, 38.46%, 48.65%, and 43.92%, respectively. As the α-ferrite precipitation process advances, the hot ductility drops and then picks up, with the minimum occurring near f_α = 10~15%. From the currently available resources, R_A > 35~40% [42,43], 60% [10,44–46], and 75% [47] are widely adopted as the critical values

for evaluating the crack sensitivity. Adopting $R_A > 60\%$ as the evaluation criterion, hot ductility returns to a higher level once $f_\alpha > 40\sim45\%$, as shown in Figure 8b.
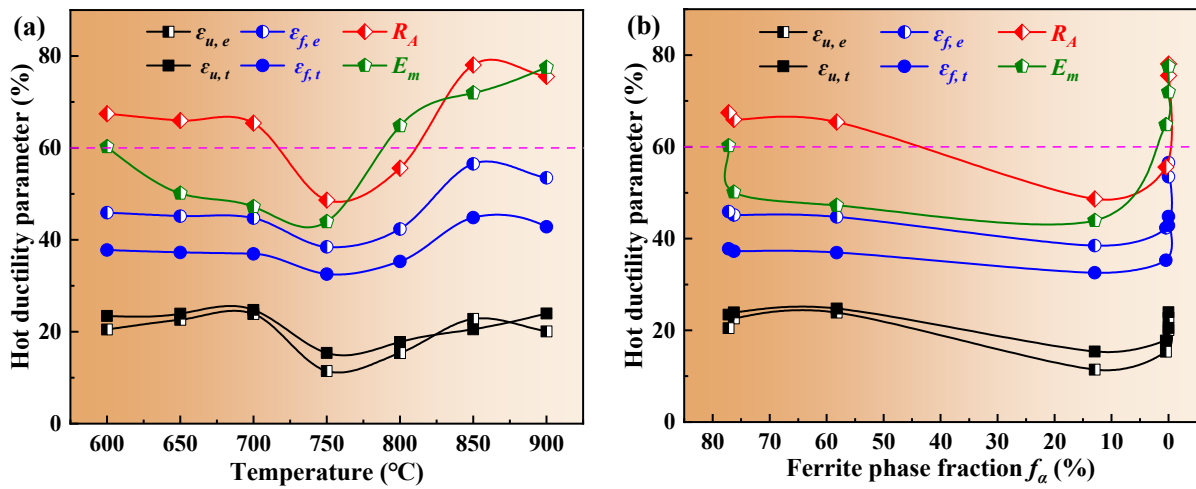

Figure 8. Variation of hot ductility parameters with α-ferrite precipitation process advances: (**a**) As functions of temperature; (**b**) As functions of f_α.

According to Figures 5 and 8 and Table 1, the temperatures 800 °C, 750 °C, and 700 °C can be considered to represent the α-ferrite start precipitation temperature, the temperature with the highest crack sensitivity, and the hot ductility recovery temperature, respectively. Tensile fracture morphology at these three typical temperatures is provided as a supplement in Figure 9. The fracture at 800 °C exhibits both dimple and polyhedral morphology, which indicates that the fracture is both ductile and brittle. Conversely, the fracture at 750 °C clearly shows the polyhedral morphology of every grain, which is typical of brittle fracture characteristics. For the experiment at 700 °C, the specimens display dimple-like fracture features with a substantial improvement in hot ductility, which is consistent with the results shown in Figure 8.
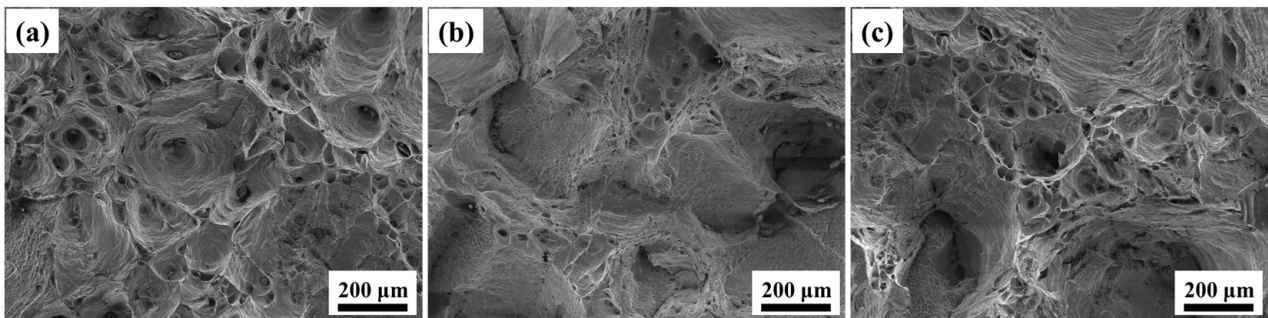

Figure 9. Fracture morphology at typical temperatures: (**a**) 700 °C; (**b**) 750 °C; (**c**) 800 °C.

In addition, the corresponding microstructures at the three temperatures are shown in Figure 10. A small amount of film-like ferrite has appeared at the austenite grain boundary near 800 °C. The average thickness of the film-like ferrite at 750 °C has reached a maximum value of 15~20 μm as the α-ferrite precipitation process advances, which is consistent with the in situ observation in Figure 3c. Nonetheless, at a reduced tensile temperature of 700 °C, substantial amounts of needle-like ferrite are observed inside the austenite, which represents that the content has reached a considerable level.
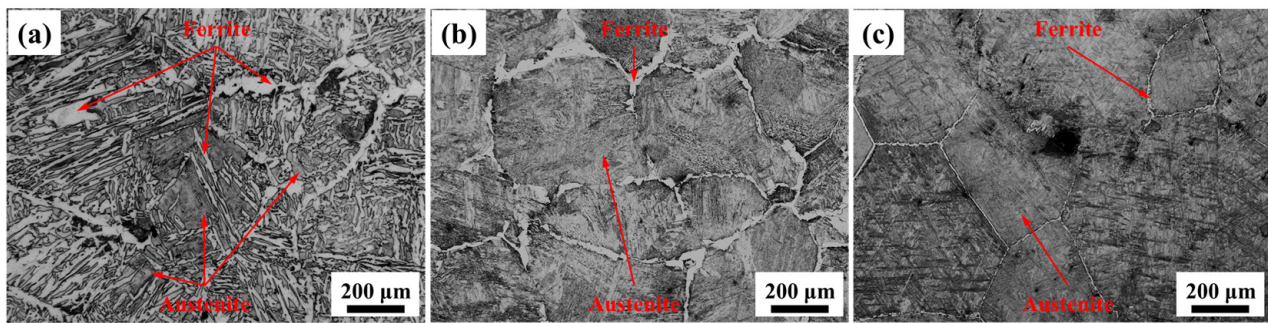
Figure 10. Microstructure at typical temperatures: (**a**) 700 °C; (**b**) 750 °C; (**c**) 800 °C.

With the pursuit of high-quality steel, the re-improvement of mechanical properties while avoiding cracks in the casting slab has become a further ambition. The development of tensile and yield strengths during the austenite phase transition is given in Figure 11. The tensile and yield strength obtained from the engineering stress-strain curve is denoted as $\sigma_{b,e}$ and $\sigma_{s,e}$, respectively. As a distinction, the tensile and yield strength under the true stress-strain curve is noted as $\sigma_{b,t}$ and $\sigma_{s,t}$. The tensile and yield strength, whichever way they were obtained, show a fairly similar pattern of evolution. In the high-temperature austenite phase region and the initial stage of α-ferrite precipitation (i.e., 750~900 °C), the high-temperature strength is not sensitive to temperature fluctuation, primarily due to the combined effect of the crystal structure and the transition of the magnetic state [33]. The tensile strength and yield strength start to improve significantly below 750 °C. At the end of the α-ferrite precipitation (600 °C), the tensile $\sigma_{b,e}$ and yield strength $\sigma_{s,e}$ are increased by about 147% and 158%, respectively, compared with those at the initial stage (800 °C).
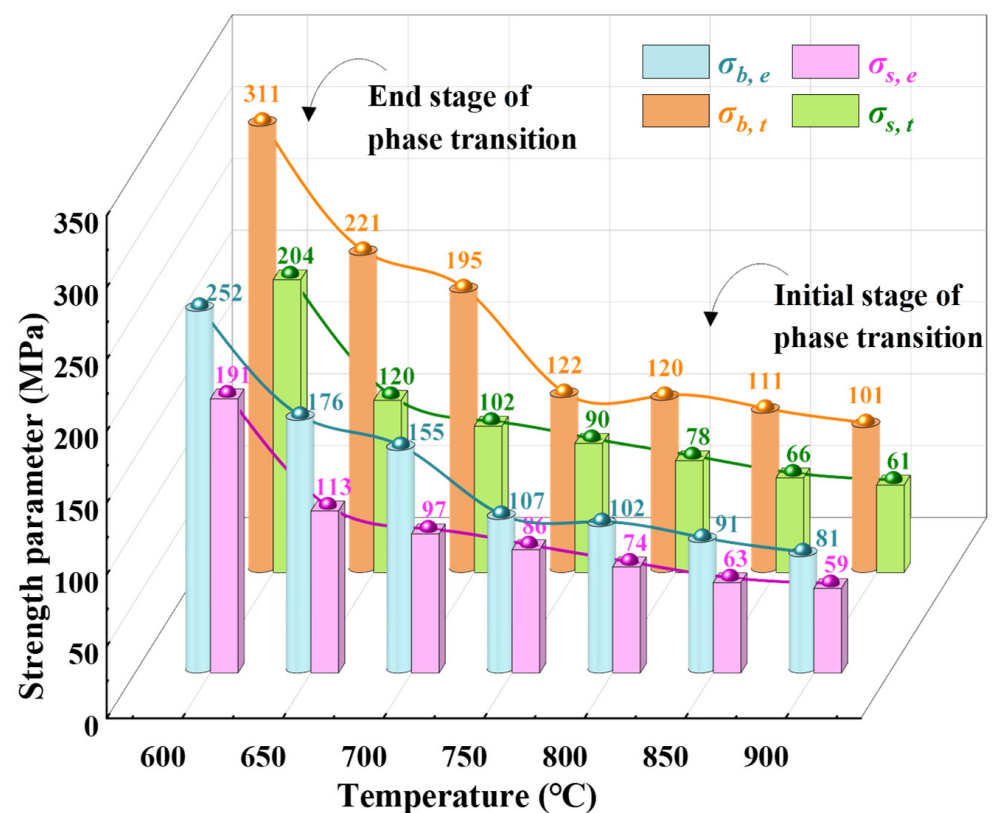

Figure 11. Relationship between high-temperature strength and test temperature during austenite phase transition process.

3.4. Effect Mechanism of α-Ferrite Sustained Precipitation on High-Temperature Properties

The effect mechanism of the α-ferrite precipitation process on high-temperature properties is summarized in Figure 12. The evolution of microstructure and properties during the cooling process is divided into three stages. (I) In the region above the temperature $T^{\alpha}_{10\%-15\%}$, the precipitate clusters at austenite grain boundaries provide nucleation sites for the formation of α-ferrite in the high-temperature region [12–15,48,49]. As the temperature decreases, film-like ferrite gradually grows at the austenite boundary. The continuity of the matrix is disrupted due to the generation of precipitate and film-like ferrite near the austenite grain boundaries. The hard precipitates and low-strength film-like ferrite induced an increase in the local strain concentration near the grain boundaries during the tensile process, which decreases rapidly in the hot ductility as the average thickness of the ferrite film increases. The average thickness of the ferrite film reaches a maximum of 15~20 μm when the ferrite content reaches 10~15% (as shown in Figures 3, 5 and 10), which renders the casting slab highly susceptible to cracking (as shown in Figure 8). (II) With the further advancement of the α-ferrite precipitation process, ferrite is rapidly generated perpendicular to the original austenite grain boundaries, leading to the emergence of a considerable number of fine ferrite grains, and the size of the original austenite grains is also gradually reduced during the phase transitions. The considerable amounts of needle-like ferrite and fine grains cause a decrease in the local strain concentration and crack extension rate, which triggers a quick increase in the hot ductility and strength at the same time and returns to a high level when $f_{\alpha} > 40$~45%. (III) Pearlite starts to precipitate at the end of the α-ferrite precipitation, and the final microstructure consists of ferrite and pearlite together. At this time, the properties of the as-cast slab are closely related to the temperature, and the strength difference between the matrix phases decreases, so the hot ductility change tends to stabilize. It is worth noting that the high-temperature strength at this stage exhibits a high correlation with temperature fluctuations, essentially due to the decrease in atomic activity as a result of the lower temperature.
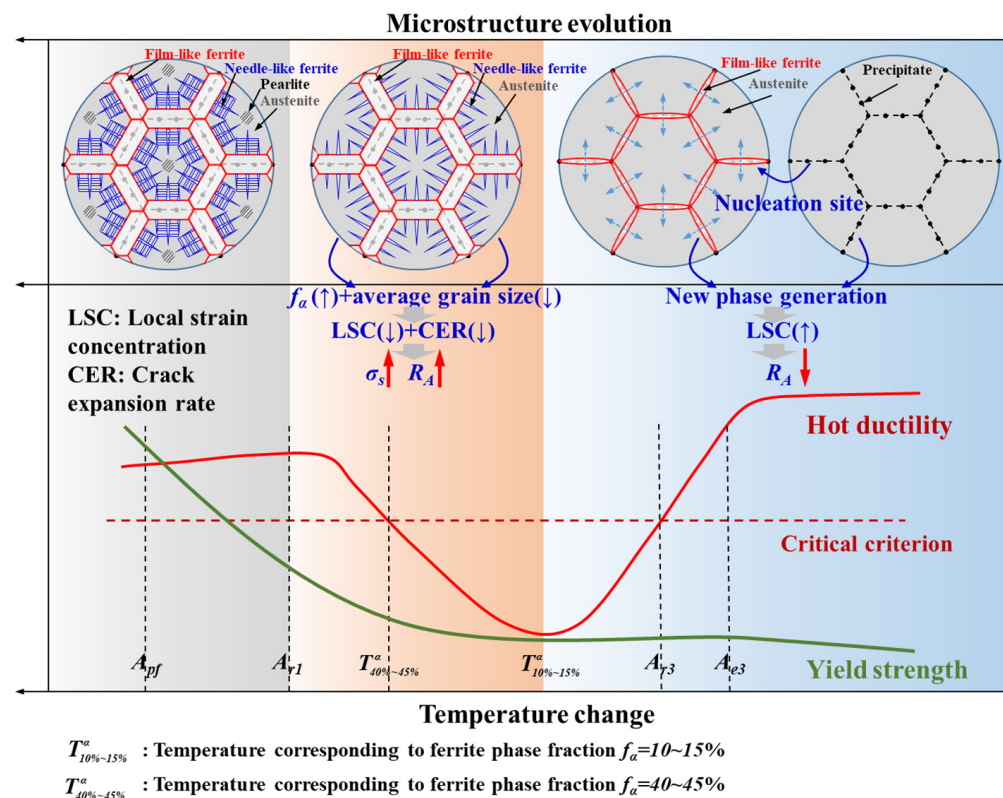

Figure 12. Effect mechanism of the α-ferrite precipitation process on hot ductility and high-temperature strength.

4. Conclusions

In this study, the α-ferrite precipitation process during continuous casting of peritectic steel has been quantified through in situ observation, high-temperature thermal expansion, and thermal tensile testing, revealing the mechanism of the α-ferrite sustained precipitation process on the high-temperature property. The conclusions of the study are as follows:

(1) The film-like ferrite precipitated along the austenite grain boundaries at the initial stage of the α-ferrite precipitation. Then, the needle-like ferrite was perpendicular to the austenite grain boundaries of rapid growth when the average thickness of the ferrite film reached 15~20 μm, and finally, the "bridging" phenomenon between neighboring needle-like ferrite marks the general completion of the ferrite transition.

(2) The temperature interval of the austenite phase is 560~804 °C, with a ferrite phase fraction of 12.95% at 750 °C and 58.25% at 700 °C. The microstructure at the end of the austenite phase transition consists of 77.21% ferrite + 22.79% pearlite.

(3) As the α-ferrite precipitation process advances, the hot ductility of the as-cast slab first decreases and then recovers, with the minimum value occurring near f_α = 10~15% and recovering to higher levels after f_α > 40~45%. Compared to the initial stage, the tensile and yield strengths at the end of α-ferrite precipitation are elevated by about 147% and 158%, respectively.

(4) The low-strength film-like ferrite in the initial stages of the α-ferrite precipitation disrupts the matrix continuity and causes serious localized strain concentrations. As the α-ferrite precipitation advances, the appearance of a considerable amount of needle-like ferrite and the grain size refinement induce reductions in the local strain concentration and crack extension rate. This phenomenon is the primary reason for the improvement in high-temperature properties.

References

1. Li, Q.; Lan, P.; Wang, H.; Ai, H.; Chen, D.; Wang, H. Formation and control of the surface defect in hypo-peritectic steel during continuous casting: A review. *Int. J. Miner. Metall. Mater.* **2023**, *30*, 2281–2296. [CrossRef]
2. Wang, Y.; Ren, Q.; Zhang, L.; Yang, X.; Yang, W.; Ren, Y.; Zhang, H. Formation and control of transverse corner cracks in the continuous casting slab of a microalloyed steel. *Steel Res. Int.* **2021**, *92*, 2000649. [CrossRef]
3. An, J.; Cai, Z.; Zhu, M. Effect of titanium content on the refinement of coarse columnar austenite grains during the solidification of peritectic steel. *Int. J. Miner. Metall. Mater.* **2022**, *29*, 2172–2180. [CrossRef]
4. Azizi, G.; Thomas, B.; Zaeem, M. Review of peritectic solidification mechanisms and effects in steel casting. *Metall. Mater. Trans. B* **2020**, *51*, 1875–1903. [CrossRef]
5. Azizi, G.; Thomas, B.; Zaeem, M. Prediction of thermal distortion during steel solidification. *Metals* **2022**, *12*, 1807. [CrossRef]
6. Zhu, M.; Cai, Z. Formation mechanism and control technology of transverse corner cracks during slab continuous casting of microalloyed steels. *Steel Res. Int.* **2023**, *94*, 2300119. [CrossRef]

7.   Ai, S.; Long, M.; Guo, W.; Liu, P.; Chen, D.; Dong, Z.; Zhang, Y.; Duan, H. Ab initio study on continuous evolution of mechanical properties in phase transition region of low carbon steel. *Steel Res. Int.* **2020**, *91*, 2000070. [CrossRef]

8.   Zhou, Q.; Yin, Y.; Liu, Z.; Zhang, J.; Zhang, J. Research mechanism of formation on transverse corner cracks in the continuous casting slab of peritectic steel. *Steel Res. Int.* **2022**, *93*, 2200336. [CrossRef]

9.   Brimacombe, J.; Sorimachi, K. Crack formation in the continuous casting of steel. *Mater. Trans. B* **1977**, *8*, 489–505. [CrossRef]

10.   Hori, S.; Suzuki, M.; Unigame, Y. Effect of carbon on the low temperature brittleness of iron. *J. Jpn. Inst. Met.* **1980**, *44*, 138–143. [CrossRef]

11.   Suzuki, H.; Nishimura, S.; Imamura, J.; Nakamura, Y. Hot ductility in steels in the temperature range between 900 and 600 °C related to the transverse facial cracks in the continuously cast slabs. *Tetsu-to-Hagané* **1981**, *67*, 1180–1189. [CrossRef] [PubMed]

12.   Cai, Z.; An, J.; Cheng, B.; Zhu, M. Effect of austenite grain size on the hot ductility of Nb-bearing peritectic steel. *Metall. Mater. Trans. A* **2023**, *54*, 141–152. [CrossRef]

13.   Sun, L.; Liu, X.; Xu, X.; Lei, S.; Li, H.; Zhai, Q. Review on niobium application in microalloyed steel. *J. Iron Steel Res. Int.* **2022**, *29*, 1513–1525. [CrossRef]

14.   Ma, F.; Wen, G.; Tang, P.; Han, J. Research present of corner transversal crack on the Nb, V and Ti micro-alloyed steel slab. *Mater. Rep.* **2010**, *24*, 89–91.

15.   Lekganyane, K.; Mostert, R.; Siyasiya, C.; Banks, K. Irreversible loss of hot ductility following simulated primary cooling of a C–Mn steel to temperatures above the ferrite transformation temperature. *Mater. Sci. Eng. A* **2021**, *810*, 141007. [CrossRef]

16.   He, G.; Wan, S.; Jiang, B.; Zhang, C.; Liu, Y.; Wu, C. Adverse effect of niobium and boron on hot deformation behavior of sulfur-containing steel. *J. Iron Steel Res. Int.* **2024**, *31*, 252–263. [CrossRef]

17.   Maehara, Y.; Ohmori, Y. The precipitation of AlN and NbC and the hot ductility of low carbon steels. *Mater. Sci. Eng.* **1984**, *62*, 109–119. [CrossRef]

18.   Thomas, B.; Brimacombe, J.; Samarasekera, I. The formation of panel cracks in steel ingots: A state-of-the-art review. *ISS Trans.* **1986**, *7*, 7–20.

19.   Comineli, O.; Abushosha, R.; Mintz, B. Influence of titanium and nitrogen on hot ductility of C–Mn–Nb–Al steels. *Mater. Sci. Technol.* **1999**, *15*, 1058–1068. [CrossRef]

20.   Cai, Z.; Zhu, M. *The Control Technology for Slab Surface Crack during Continuous Casting of Micro-Alloyed Steel*; Metallurgical Industry Press: Beijing, China, 2021.

21.   Zhao, S.; Wu, Y.; He, M.; Zhang, L. Effects of cooling rates on microstructures and mechanical properties of Nb-Ti microalloyed steel. *J. Shanghai Jiaotong Univ. Sci.* **2012**, *17*, 653–657. [CrossRef]

22.   Ma, F.; Wen, G.; Tang, P.; Yu, X.; Li, J.; Mei, F. Causes of transverse corner cracks in microalloyed steel in vertical bending continuous slab casters. *Ironmak. Steelmak.* **2010**, *37*, 73–79. [CrossRef]

23.   Yang, X.; Zhang, L.; Li, S.; Li, M. Influence of cooling conditions on the hot ductility of Nb-Ti-bearing steels. *Metall. Res. Technol.* **2015**, *112*, 604. [CrossRef]

24.   Mintz, B. Understanding the low temperature end of the hot ductility trough in steels. *Metall. Res. Technol.* **2008**, *24*, 112–120. [CrossRef]

25.   Mintz, B.; Lewis, J.; Jonas, J. Importance of deformation induced ferrite and factors which control its formation. *Metall. Res. Technol.* **1997**, *13*, 379–388. [CrossRef]

26.   Mintz, B.; Abu-Shosha, R.; Shaker, M. Influence of deformation induced ferrite, grain boundary sliding, and dynamic recrystallisation on hot ductility of 0·1–0·75% C steels. *Metall. Res. Technol.* **1993**, *9*, 907–914. [CrossRef]

27.   Mintz, B.; Abushosha, R.; Jonas, J. Influence of dynamic recrystallisation on the tensile ductility of steels in the temperature range 700 to 1150 °C. *ISIJ Int.* **1992**, *32*, 241–249. [CrossRef]

28.   Qian, G.; Cheng, G.; Hou, Z. Effect of the induced ferrite and precipitates of Nb–Ti bearing steel on the ductility of continuous casting slab. *ISIJ Int.* **2014**, *54*, 1611–1620. [CrossRef]

29.   Liu, Y.; Sun, Y.; Wu, H. The crack generation and propagation during $\gamma \rightarrow \alpha$ transformation in Nb-microalloyed steel. *Metall. Res. Technol.* **2020**, *36*, 868–876. [CrossRef]

30.   Ai, S.; Long, M.; Yang, X.; Chen, D.; Duan, H. Prediction model for crack sensitive temperature region and phase fractions of slab under continuous casting cooling rates based on finite number of experiments. *J. Mater. Res. Technol.* **2023**, *22*, 1103–1117. [CrossRef]

31.   Dou, K.; Meng, L.; Liu, Q.; Liu, B.; Huang, Y. Influence of cooling rate on secondary phase precipitation and proeutectoid phase transformation of micro-alloyed steel containing vanadium. *Met. Mater. Int.* **2016**, *22*, 349–355. [CrossRef]

32.   Jiménez-Lugos, J.; Cabrera-Marrero, J.; Chávez-Alcalá, J.; Hallen-López, J.; López-Rodríguez, J. Constitutive modeling of hot deformation of carbon steels in the intercritical zone. *Mater. Res.* **2022**, *25*, e20210275. [CrossRef]

33.   Ai, S.; Long, M.; Zhang, S.; Chen, D.; Dong, Z.; Liu, P.; Zhang, Y.; Duan, H. Ab initio calculations on elastic properties of IF steel matrix phase at high temperature based on lattice expansion theory. *Metals* **2020**, *10*, 283. [CrossRef]

34.   Mintz, B. The influence of composition on the hot ductility of steels and to the problem of transverse cracking. *ISIJ Int.* **1999**, *39*, 833–855. [CrossRef]

35.   Abushosha, R.; Comineli, O.; Mintz, B. Influence of Ti on hot ductility of C-Mn-Al steels. *Mater. Sci. Technol.* **1999**, *15*, 278–286. [CrossRef]

36.   Shin, E. Hot Ductility of TWIP Steels. Ph.D. Thesis, City University, London, UK, 2014.

37. Calvo, J.; Rezaeian, A.; Cabrera, J.; Yue, S. Effect of the thermal cycle on the hot ductility and fracture mechanisms of a C–Mn steel. *Eng. Fail. Anal.* **2007**, *14*, 374–383. [CrossRef]

38. Mintz, B.; Arrowsmith, J. Hot-ductility behaviour of C–Mn–Nb–Al steels and its relationship to crack propagation during the straightening of continuously cast strand. *Met. Technol.* **1979**, *6*, 24–32. [CrossRef]

39. De Andres, C.; Caballero, F.; Capdevila, C.; Álvarez, L. Application of dilatometric analysis to the study of solid–solid phase transformations in steels. *Mater. Charact.* **2002**, *48*, 101–111. [CrossRef]

40. Liu, T.; Long, M.; Fan, H.; Chen, D.; Chen, H.; Duan, H.; Jiang, W.; He, W. Dilatometric determination of four critical temperatures and phase transition fraction for austenite decomposition in hypo-eutectoid steels using peak separation method. *J. Mater. Res.* **2018**, *33*, 967–977. [CrossRef]

41. Barbier, D.; Guérin, J.; Dubar, M.; Bénard, T.; Bonneau, S.; Cabrera, E. Hot ductility and flow stress of AISI 4130 and 52100-type steels. *Mater. Sci. Eng. A* **2017**, *690*, 37–43. [CrossRef]

42. Mintz, B.; Qaban, A. The influence of precipitation and high levels of Al, Si, P as well as a small B addition on the hot ductility of TWIP and TRIP assisted steels: A critical review. *Metals* **2022**, *12*, 502. [CrossRef]

43. Mintz, B.; Crowther, D. Hot ductility of steels and its relationship to the problem of transverse cracking in continuous casting. *Int. Mater. Rev.* **2010**, *55*, 168–196. [CrossRef]

44. Suzuki, H.; Nishimura, S.; Yamaguchi, S. Physical simulation of the continuous casting of steels. In Proceedings of the Conference on Physical Simulation Techniques for Welding, Hot forming and Continuous Casting, Canmet, Ottowa, ON, Canada, 2−4 May 1988.

45. Guo, Y.; Zhao, Y.; Wang, K.; Song, S. A comparative study of hot ductility of unadded and Ce-added SA508-4N RPV steels. *J. Mater. Res. Technol.* **2020**, *9*, 16038–16050. [CrossRef]

46. Guo, Y.; Wang, K.; Song, S. Abnormal influence of impurity element phosphorus on the hot ductility of SA508Gr. 4N reactor pressure vessel steel. *Mater. Sci. Eng. A* **2020**, *792*, 139837. [CrossRef]

47. Bannenberg, N.; Bergmann, B.; Jungblut, H.; Muller, N.; Reich, K. Procedures for successful continuos casting of steel microalloyed with Nb, V Ti and N. In Proceedings of the Proc. Conf. Microalloying '95, Pittsburgh, PA, USA, 11−14 June 1995; Iron and Steel Society. pp. 83–94.

48. Liu, Y.; Sun, Y.; Wu, H. Effects of chromium on the microstructure and hot ductility of Nb-microalloyed steel. *Int. J. Miner., Metall. Mater.* **2021**, *28*, 1011–1021. [CrossRef]

49. Gontijo, M.; Hoflehner, C.; Estermann, P.; Ilie, S.; Six, J.; Sommitsch, C. Effect of strain rate on the hot ductility behavior of a continuously cast Ti–Nb microalloyed steel. *Steel Res. Int.* **2020**, *91*, 2000022. [CrossRef]